

Content-adaptive Lenticular Prints

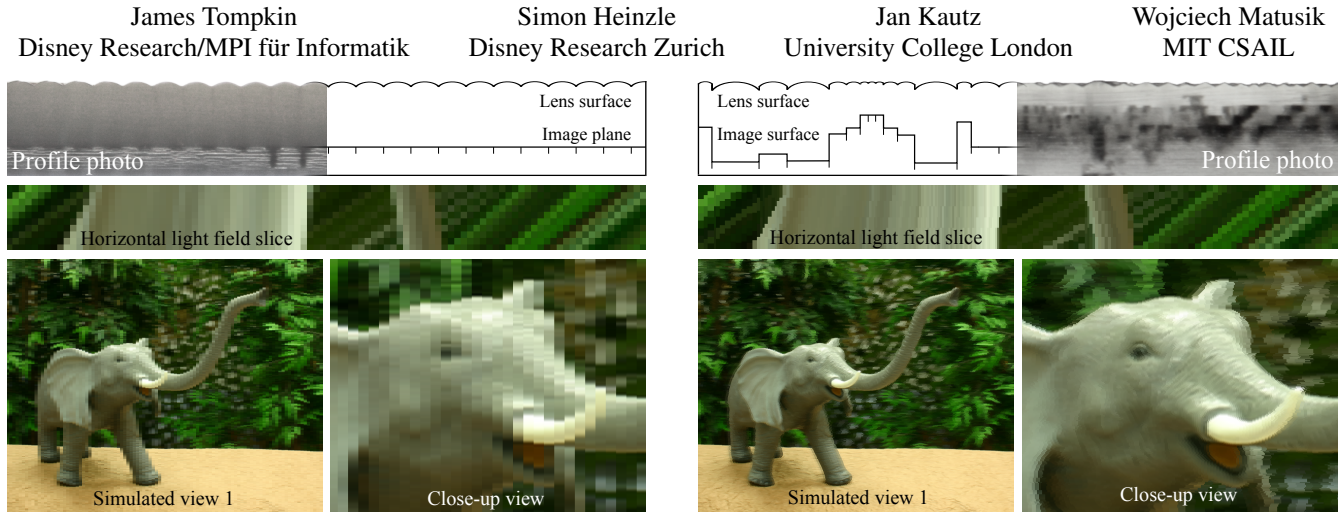


Figure 1: We exploit the varying frequency content of static light fields to optimally adapt lenslet array display patterns. Top: Two lenticular displays, printed with a multi-material printer. Left: Regular lenticular, with lens sizes chosen to maximize PSNR of the input light field. Right: Content adaptive lenticular, where our optimization process distributes a set of lenses based on a local frequency analysis of the light field. The resulting light field emitted from our display is crisper than that from a regular lenticular display, exhibits much smoother motion parallax, and results in a higher PSNR. Bottom: A slice from the emitted light fields and two simulated views.

Abstract

Lenticular prints are a popular medium for producing automultiscopic glasses-free 3D images. The light field emitted by such prints has a fixed spatial and angular resolution. We increase both perceived angular and spatial resolution by modifying the lenslet array to better match the content of a given light field. Our optimization algorithm analyzes the input light field and computes an optimal lenslet size, shape, and arrangement that best matches the input light field given a set of output parameters. The resulting emitted light field shows higher detail and smoother motion parallax compared to fixed-size lens arrays. We demonstrate our technique using rendered simulations and by 3D printing lens arrays, and we validate our approach in simulation with a user study.

CR Categories: I.3.1 [Computer Graphics]: Hardware Architecture—Three-dimensional displays;

Keywords: Lenticular displays, 3D printing.

Links: DL PDF WEB

ACM Reference Format

Tompkin, J., Heinzle, S., Kautz, J., Matusik, W. 2013. Content-Adaptive Lenticular Prints. ACM Trans. Graph. 32, 4, Article 133 (July 2013), 10 pages. DOI = 10.1145/2461912.2462011 <http://doi.acm.org/10.1145/2461912.2462011>.

Copyright Notice

Permission to make digital or hard copies of all or part of this work for personal or classroom use is granted without fee provided that copies are not made or distributed for profit or commercial advantage and that copies bear this notice and the full citation on the first page. Copyrights for components of this work owned by others than ACM must be honored. Abstracting with credit is permitted. To copy otherwise, or republish, to post on servers or to redistribute to lists, requires prior specific permission and/or a fee. Request permissions from permissions@acm.org.
Copyright © ACM 0730-0301/13/07-ART133 \$15.00.
DOI: <http://doi.acm.org/10.1145/2461912.2462011>

1 Introduction

Displays that provide the illusion of three dimensions have recently experienced a rebirth. While most commercial displays rely on special glasses, it is generally agreed that automultiscopic displays—displays able to provide 3D vision without glasses—offer significant advantages. The predominant automultiscopic technology today is based on parallax-type displays, which create the illusion of three dimensions by physically separating emitted viewing rays. Ray separation is often achieved by placing tiny lens arrays in front of an image surface. This lenticular technology is well suited to display 3D content in uncontrolled lighting environments, in contrast to other techniques such as multi-layer or holographic displays [Lueder 2012]. Lenticular arrays have constant pitch and are arranged on a regular grid to accommodate the maximum possible depth. However, three dimensional scenes often do not cover all depth ranges throughout the scene, and local patches of the scene might be better represented using different lens arrangements.

We introduce content-adaptive lenticular prints: a method for static displays which uses a modified lens array optimized to a static input light field. Our approach is motivated by the observation that light fields generated from real world scenes often show locally-varying angular and spatial frequency content. Therefore, a regular lenticular arrangement using one type of lens often cannot reproduce such light fields efficiently, and parts of these light fields could be represented better using different lens sizes and arrangements if we could exploit the varying frequency content.

We achieve this by computing an optimal arrangement of different lens sizes based on an analysis of the input light field. Our discrete optimization algorithm distributes a precomputed set of lenslets according to the angular and spatial frequencies of the input light field to generate a lenticular print with improved angular and spatial resolution over regular samplings. To maximize vertical spatial resolution, our algorithm supports 1D horizontal parallax which is sufficient to support stereoscopic viewing. In addition to the distribution algorithm, we determine an optimal set of input lenses given spe-

cific manufacturing limits. Further, we employ additive 3D multi-material printing technology to manufacture physical prototypes of the proposed content-adaptive lenslets. Using 3D printing, we are able to introduce general-purpose lenticular display features such as view-blockers using baffles, non-planar image surfaces, and oriented lenses for better field of view usage. We demonstrate the improved reproduction quality with simulated results as well as with proof-of-concept physical prototypes.

Our contributions are:

- A light field analysis and optimization strategy to yield the ideal layout of 1D lenslets which trades between spatial and angular resolution for a given static scene.
- Optimized lenses for 3D-printing automultiscopic displays.
- 3D-printed prototypes of content-adaptive lenticular displays.

2 Related Work

Autostereoscopic and multi-view display technology has been extensively researched, and continues to be a prominent research field. Lueder [2012] presents a recent overview on the huge body of related work. We focus on lenticular displays for integral imaging, parallax barrier type displays, and multi-layer light field displays.

Integral Imaging Lippmann [1908] proposed a small array of lenticular lenses to acquire an incident light field onto a film plane, a process being revived currently in so-called light field cameras. The same film plane with the same lenses forms a 3D display that emits the captured light field. Many improvements to Lippmann's basic idea have been proposed, and a thorough overview of recent advances is given Kim et al. [2010]. For instance, apparent resolution can be enhanced by using slanted lenticular sheets arranged with respect to LCD subpixels [Berkel 1999] or by spatio-temporal multiplexing [Jang and Javidi 2002]. Kim et al. [2005] demonstrate curved lenticulars for wider viewing angles, whereas Takahashi et al. [2006] propose holographic lens elements to increase field of view. Park et al. [2005] propose using two layers of lenslets with different sizes and focal lengths to increase the number of possible rays. Said and Talvala [2009] propose a multi-projector system to improve quality. In contrast, Fuchs et al. [2008] present a regular lenticular display system which additionally relies on the incident illumination angles to support ambient lighting-dependent effects.

Ueda et al. [2008] propose an adaptive integral imaging camera system using programmable lenses which can individually change their field of view. Kao et al. [2009] present a display that changes the focal length of all lenses simultaneously to adapt to the viewer's distance. Jang and Javidi [2003] present an acquisition and display system where multiple lenses with different focal lengths and apertures in a fixed, semi-regular lenslet array are interleaved in space and time by rapid movement. Kim et al. [2011] present a similar acquisition system using a fixed, stationary, semi-regular lenslet array, which could also be used for integral image displays. Both strategies increase resolution and depth of field; however, the lens arrangement is not optimized for a given scene and therefore sub-optimal. To our knowledge, no related works have tried to find an optimal spatial/angular resolution trade-off for a given light field.

Parallax Barriers Ives [1903] proposed one of the first parallax barrier multi-view displays, where a blocking pattern in front of an image surface provides different views for different viewing angles. Using LCD technology, Isono et al. [1993] proposed a dynamic parallax barrier to adapt the barrier pattern based on the number of users and their positions. Time-multiplexed parallax barriers [Kim et al. 2007] can improve the perceived spatial sampling resolution. Stereoscopic content can be adapted to the viewer's po-

sition by tracking their location [Perlin et al. 2000; Peterka et al. 2008]. The Random Hole Display [Nashel and Fuchs 2009] randomizes the barrier pattern, replacing interference between views with high frequency noise which is visually less objectionable. The displays of Cossairt et al. [2007] and Jones et al. [2007] show a 360° light field of a scene. While termed volumetric displays, they are similar to parallax barrier displays. Instead of using a blocking pattern to direct different rays to different angles, the content is time-multiplexed onto a rotating mirror with a high-speed projector.

Holography Holography [Schnars and Jüpter 2005; Zebra Imaging 2013] uses the interference of two laser beams to record a light field. While holography can produce excellent results, there are clear limitations. Holograms require a point light positioned at a specific location to reproduce the light field. Due to relatively high light absorption, the point light needs to be very bright compared to the environment lighting. This makes holograms difficult to use outdoors. In contrast, lenticular technology can use reflected light and backlighting at much better light efficiency, making it easier to use in uncontrolled environments with area lights.

Multi-layer Light Field Displays Lanman et al. [2010] improve on parallax barrier displays by using modulation instead of blocking barriers. The modulation pattern is dynamically adapted based on a factorization of the light field, which results in higher resolution and brightness when compared to traditional parallax barrier approaches. Wetzstein et al. [2011] extend this approach to multiple modulating layers, where the layer contents are computed using tomographic reconstruction techniques. The layered display is able to reproduce a very high spatial resolution with good ranges of depth. Lanman et al. [2011] reformulate the problem to switching LCDs instead of modulating layers and show a real-time prototype using multiple stacked LCD screens. Holroyd et al. [2011] present a related multi-layer display based on blocking display layers instead of modulating ones. Wetzstein et al. [2012] propose a general framework for displays comprising time-multiplexed, light-attenuating layers illuminated by uniform or directional backlighting. The main advantage is reduced artifacts and wider field of views than previous multi-layer displays. While not a light field display, Sajadi et al. [2012] use multi-layer LCDs and an optical pixel sharing unit in a projection system to provide resolution enhancement.

Light Field Analysis Chai et al. [2000] presented the first analysis on the sampling requirements for light field signals, and Durand et al. [2005] extended their work to a fundamental analysis of light transport and its sampling requirements. Based on both analyses, Zwicker et al. [2006; 2007] determine the limits of light field displays and introduce effective anti-aliasing strategies. One of the basic findings of their work is the trade-off between spatial and angular resolution, on which our optimization is based. This analysis was later extended to include aliasing on light field displays in the presence of visual crosstalk [Jain and Konrad 2007; Ramachandra et al. 2011], where a sharpening pre-filter was proposed to reduce the effects. Hachisuka et al. [2008] introduced optimized adaptive sampling strategies for light field generation using raytracing. Lehtinen et al. [2011] exploit preceding light field analysis to efficiently and adaptively sample and reconstruct multi-dimensional signals in ray-tracing. Our light field analysis differs as our goal is to determine the best angular and spatial resolution trade-off.

Lens Design and Printed Optics While a broad body of work for lens-system design exists [Smith 2007], few papers focus on the optimal design of lenses for automultiscopic viewing: Johnson and Jacobsen [2005] discuss lenticular sheet manufacturing technologies and propose elliptically-shaped lenses to reduce cross-talk. Micro lenses has been successfully printed using an approach similar to ink-jet printing (e.g., see [Cox et al. 2001; Cruz-Campa et al.

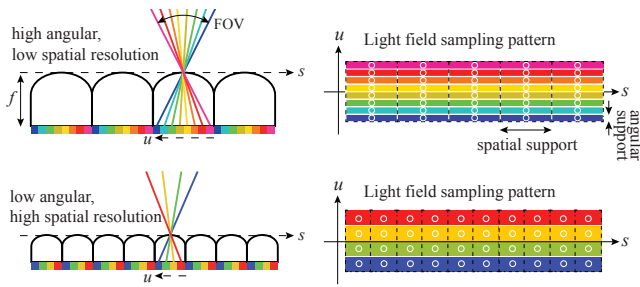


Figure 2: Left: Lenticular lens array. Different viewing directions are multiplexed to different pixels on the image plane, creating an automultiscopic display. Right: The (s, u) sampling pattern of the lenslet array (2D light field). The width of the lens defines its extent in the spatial (s) domain. The focal length f and width define the field of view of the lens, which in turn defines the angular (u) support. The angular sampling pattern becomes denser when traded against spatial resolution with a constant field of view. The u samples are defined relative to their associated s sample.

2010], where small droplets are dispersed onto a substrate). However, these technologies generate a tiny lens for each droplet and are not applicable to larger lenses. To our knowledge, bigger lenses have not been manufactured using printing technology. Very recently, Willis et al. [2012] print embedded custom optical elements to achieve interactive devices that are 3D printed in their entirety. Our approach extends their vision by augmenting printed devices with stereo display capabilities. Papas et al. also extend their optimization techniques for goal-based caustics [2011] to handle configurations of planar refractive surfaces for magic lenses [2012].

3 Lenticular Displays

We summarize the principle of automultiscopic displays based on lenticular arrays, and for this we assume that each lens can be modeled as a perfect pinhole. Figure 2 shows one line of such a display: different viewing directions are angularly multiplexed through the lens and are mapped to different pixels on the image plane. An observer at some distance from the lens array will see different pixels for different positions along the horizontal axis and will perceive motion parallax as well as stereoscopic depth cues.

Following the notation of Zwicker et al. [2006], the lens array emits an output light field that can be characterized by a spatial and angular pattern (s, u) (Figure 2). The angular sampling points are defined relative to their respective spatial sampling points. In other words, s denotes the origin of the ray, whereas u describes the direction of the emitted ray, such that each lens defines a spatial sampling location and emits multiple angular samples from the image plane. The spatial sampling density is defined by the lens width, whereas the angular sampling density is characterized by the focal length f and the underlying pixel density. Each column in the (s, u) plot denotes one lens, and each row denotes a set of parallel rays.

The exact sampling densities can be arbitrary, but are often bound by the possible resolution of the image surface as well as the optical qualities of the employed lenses. Figure 2 shows two different configurations, assuming a constant image surface density and a constant field of view. Increasing the width of individual lenses increases the number of angular samples and, subsequently, supports more angular variation. Increased angular resolution comes at the cost of reduced spatial resolution, which is a fundamental trade-off for current lenticular and parallax-barrier based displays.

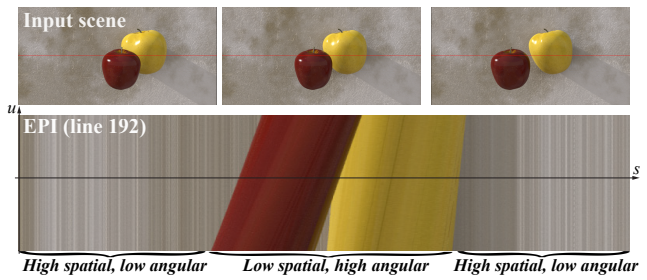


Figure 3: The local angular and spatial frequency content of light fields often differs considerably. Top: Three frames of a scene. The background wall is positioned approximately at the focal plane of the display, and the two apples float in front of the focal plane. Bottom: The frequencies for one line of the input light field (red line in input images) shown in epipolar plane image (EPI) representation. The angular frequencies of the wall are very low, whereas its spatial frequencies are very high. In contrast, the red apple features high angular frequencies and low spatial frequencies.

4 Content-adaptive Lenticular Displays

All current lenticular displays are based on regular (s, u) sampling patterns. However, the local angular and spatial frequencies of natural light fields often differ considerably, and many of the (s, u) samples are either wasted or not optimally placed for a given light field. Figure 3 shows an example where a textured wall is located at the focal plane. As a result, the angular frequency content of each point on the wall is low (all viewing directions see the same color), but the spatial frequency content is high (the wall is textured). The objects in front of the plane require much less spatial frequency and much more angular frequency due to their distance from the display.

This insight motivates our approach: while objects close to the focal plane would ideally have lenses with low angular variation (i.e., lens width of one pixel), objects further away from the focal plane would benefit from larger lenses. Therefore, we propose to locally adjust the lenses to better replicate the input light field. We achieve this by distributing lenses of varying size in conjunction with optimizing the image pattern such that the light field emitted from the display generates the least error compared to the input light field.

4.1 Discrete Light Field Optimization

Our goal is to find a lens distribution that generates an output light field ℓ_{out} which matches an input light field ℓ_{in} as close as possible:

$$L_o = \arg \min_L (\text{norm}(\ell_{\text{in}}, \ell_{\text{out}}(L))), \quad (1)$$

where $L_o = \{l_i | i = 1..n\}$ denotes the optimal lens distribution, and $\text{norm}()$ can be any appropriate norm (e.g., L2 or gradient based). Each lens $l_i = \{w_i, c_i, p_i\}$ is characterized by its width w_i , the color content of the image surface c_i , and the lens parameters p_i such as the focal length. The field of view of all lenses and the resolution of the color content are kept constant across the whole display. As a result, the angular resolution of a lens increases with its width w_i .

Solving for the optimal distribution given a discrete set of lenses is a packing problem, similar to the knapsack problem. However, in our case, the weights are not known a priori as each lens will result in a different error depending on its placement. Therefore, we propose a bottom-up dynamic programming approach to find an optimal distribution L_o for an input light field ℓ_{in} , where our algorithm recursively determines the best lens configuration for larger and larger subsets of ℓ_{in} . In each recursion step, we place all lenses from the

Algorithm 1: $e = \text{computeLensDistribution}(\ell_{\text{in}})$

```

for all possible candidate lenses  $l_i$ 
  // Compute error for placing lens  $l_i$  on right-hand side of  $\ell_{\text{in}}$ 
   $e_i = \text{error}(l_i \cap \ell_{\text{in}})$ 
  // Add lowest possible error for remainder of  $\ell_{\text{in}}$ 
   $e_i = e_i + \text{computeLensDistribution}(\ell_{\text{in}} \setminus l_i)$ 
return lens  $l_i$  with lowest error  $e_i$ 

```

set of candidate lenses at the right-hand side of the input light field and compute the error (Equation 1) over their extent. Then, our goal is to find the lens distribution which minimizes the error for the remaining left-hand side of the input light field. We recurse, and perform the same procedure on the remaining left-hand side subset of the light field not covered by the initial lens placement. The recursion continues until the width of the remaining left-hand side is equal to the smallest candidate lens. The error induced by the final lens placement is propagated up and at each stage of recursion the lens arrangement with the lowest error is selected. The memoization step in our dynamic programming algorithm is the storage of the error sums and corresponding lens distributions for the left-hand side recursion widths. As we solve for horizontal parallax only, our algorithm can be evaluated independently on single scanlines. Algorithm 1 summarizes our optimization; more detailed pseudocode and an example run are given in the supplemental material.

The error that a lens incurs follows the same metric as defined in Equation 1, but it is computed only over the subset of the light field covered by the lens. Therefore, Algorithm 1 will provide an optimal solution for Equation 1. Our optimization employs an L2 error norm: the squared difference between input and output ray colors defines the error for a given lens at a given position. Perceptual norms in other color spaces are possible, however, we found our results were convincing without further comparison.

Resampling and Filtering Figure 2 shows that each lens covers a number of spatial and angular samples from the input light field. These need to be resampled to the spatial-angular pixel samples of the lens. We use a box filter according to the output sampling width, so each pixel on the image surface is computed from the mean color of the input rays covered by each output sample. From a signal processing point of view, better filters would be more appropriate; however, only approximate filters could be used due to our irregular sampling structure, such as elliptical weighted average (EWA) filters or splatted filters (e.g., Lanczos). These depend on the output sampling pattern in a larger neighborhood and would ideally be applied once the output is given. Of course, the specific output is unknown until after optimization. It is possible to filter for every possible lens combination, or at optimization time, but this is computationally expensive.

To speed up the optimization, we further resample the input light field to the maximum output resolution using bicubic resampling. Therefore only one interpolation step is carried out before starting the optimization, rather interpolating for each candidate lens.

Spatial vs. Angular Weighting The L2 error can be computed directly in the light field domain; however, the angular and spatial dimensions can be re-weighted if desired. Instead of computing a 2D box filter, we compute the angular and spatial errors individually: the L2 norm is computed along the spatial direction (summing up 1D box columns) and the angular direction (summing up 1D box rows). The resulting errors are combined using a spatial-angular weighting factor, which steers the lens generation between reproducing angular and spatial variation. All our results were computed with equal weights for both dimensions, as a balanced weighting subjectively produces the best results. The supplemental material shows examples of spatial-angular weighting factor variation.

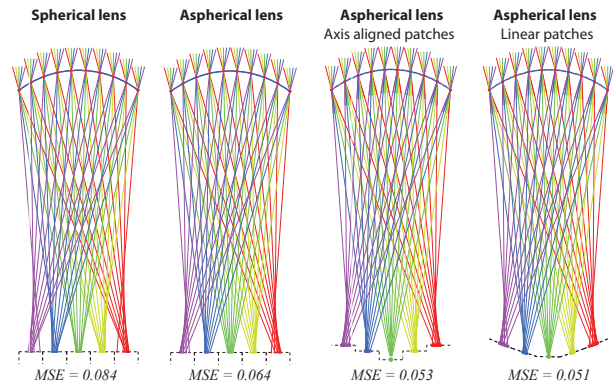


Figure 4: Raytraces through our optimized lenses, shown for a 30° field of view and a 5mm width. Each color corresponds to a set of orthographic rays; the image surface is shown beneath. Our optimization minimizes the mean squared projection error to the pixel center. Aspherical lenses show better off-axis characteristics, and with arbitrary image surfaces the error can be minimized further.

Multi-scanline Solves Our algorithm computes the optimal lens distribution for each scanline individually, which can lead to spatial noise along otherwise crisp edges. This can be mitigated by choosing similar lenses in neighboring scanlines. To this end, we extend our algorithm such that a sliding window of multiple scanlines is used to compute the lens arrangement for each particular scanline. The lens error on one scanline is then computed by summing the errors supposing the lens were also applied to neighboring scanlines in a window. This gives an increase in smoothness but a reduction in apparent resolution, for additional computational cost (Figure 7).

Algorithmic Complexity Our optimization algorithm requires $O(\|L\|n)$ space complexity as well as $O(\|L\|n)$ run-time complexity for a scanline width of n pixels and a set of candidate lenses L , where $\|L\|$ is typically less than 20. In comparison, the (exhaustive) search space is of similar size to the restricted integer partition function, which is of exponential order [Hardy and Ramanujan 1918].

4.2 Lens Optimization

To generate the desired lens arrangement from our discrete optimization, an appropriate set of candidate lenses must be determined before the full display can be generated. Given a minimum lens size and target display resolution, we first optimize for lenses of the desired widths. Our optimization searches for 1D plano-convex aspherical lenses that result in the best focusing quality across all views for a given overall field of view.

While analytical solutions for minimizing spherical aberration for the central views exist [Kweon and Kim 2007], yielding similar solutions for multiple off-center views is tedious to achieve, especially if coma aberrations are also to be minimized. Instead, we employ numerical optimization to generate the optimal lens shape given a specific lens model. More specifically, we strive to minimize the deviation of the refracted viewing rays from their ideal focus position. This deviation is computed by raytracing through the parameterized lens surface and intersecting the refracted rays with the pixel surface. The deviation error is then defined as the sum of squared distances of the intersection points to their intended pixel center. A non-linear optimization minimizes this focus error for the parameterized lens model. We investigated two different lens types: spherical lenses and aspherical lenses. In general, aspherical lenses tend to be superior to spherical lenses, especially for center views [Johnson and Jacobsen 2005]. The result of a numerical optimiza-

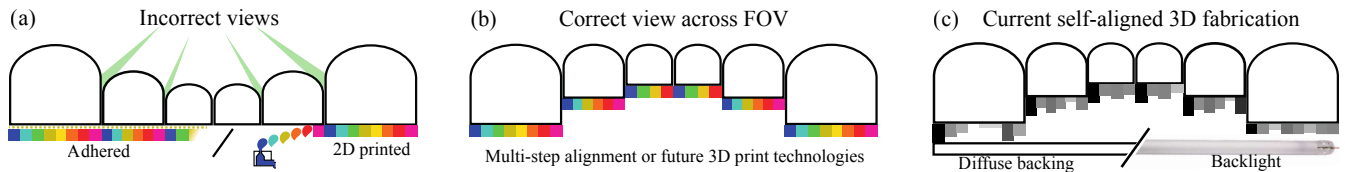


Figure 5: Fabrication alternatives. Aligned image planes across all lenses might lead to incorrect views (a). By aligning the lenses onto a plane these inconsistent views can be eliminated (b). Our current printing technology allows to print only two materials simultaneously. While one material is being used for the clear lens shape, we print varying thicknesses of a black material to achieve different shades of gray.

tion for a 5mm lens with a 30° field of view can be found in Figure 4, where we show ray-traces of both lens models and the associated average focus errors (normalized to the pixel size) from five orthographic viewing directions. More details on the lens optimization can be found in the supplemental material.

Since our fabrication procedure is quite flexible (Section 5) we propose two optimizations: to adapt the shape of the image surface, and to rotate lenses towards the primary viewing location.

Non-Planar Image Surface The optimal focusing distance for different views does not lie on a plane but rather on a curved surface [Smith 2007], and ideally the image plane should be at a different depth for different views. We incorporated alternative image plane shapes into our optimization: axis-aligned planar patches, non-axis aligned facets and parametric curves. In addition to the lens model parameters, the optimization includes parameters for the pixel heights in the case of axis-aligned patches or vertex points in the case of linear patches. Thus, the shape of the lens as well as the back surface are optimized jointly. In general, the views close to the optical axis of the lenses can be improved greatly by this optimization, whereas the off-axis views tend to perform similarly to the initial optimization result. Figure 4 shows the result of this optimization for aspherical lenses for axis-aligned and non-axis aligned facets. As can be seen from our optimization results, the resulting focus error can be reduced by 17.5% and 20.8% respectively for a material with index of refraction $n = 1.47$.

Lens Rotation Using lenses with aligned optical axes wastes many rays on the borders of the lenslet array that will fall outside the combined field of view of all lenses. Due to the lens characteristic for off-axis views, lenses on the array borders will further show increased crosstalk. To minimize these effects, we align the optical axis to the expected center position of the viewer. More specifically, the amount of rotation for each lens is chosen such that all optical axes intersect at the center position for an assumed viewer distance.

5 Fabrication

Lenticular prints usually consist of a regular lens sheet with a printed image glued underneath (Figure 5a). The lenticular sheet is usually composed of optical quality plastic resin and is typically created by extruding plastic underneath a drum shaped with the inverse of the required lens profile [Johnson and Jacobsen 2005]. Affixing the image to the lens requires pixel-accurate registration for the light field to appear correctly. As our lens arrays change shape and position over the image, existing lenticular fabrication methods are less practical. It is possible to manufacture a drum or mold to create the correct lens array shape but, as this shape changes with each input light field, it may only be economical for large print runs.

With the advent of high-accuracy 3D printing technology, our work becomes more applicable and accessible. We employ an additive multi-material printer that fabricates $16\mu\text{m}$ -accurate object layers using uv-curable resin (Objet500 Connex 3D polymer printer). As our printer is able to print two different materials simultaneously,

we chose to fabricate the lens surface simultaneously with the image surface rather than using separately printed cards. Furthermore, 3D printing also easily allows for lenses with non-planar image surfaces. Printing the lenses and the display simultaneously means that our image surface is perfectly aligned with the lens surface. Instead of producing one image surface for all lenses (shown in Figure 5a), which would introduce visual artifacts throughout the field of view of the display, we align the lens surfaces rather than the image planes to remove the crosstalk from adjacent lenses of different sizes (Figure 5b). With this approach, there are no artifacts within the field of view of the display, but beyond it the backlight will leak through these discontinuities unless baffles are printed.

A limitation of our current printer is that it is only able to print two materials at the same time. As the first material, we use a transparent resin to realize the lens shape, and we use the other material to print the display content. We choose a black material for the display content. Since the cured black resin is translucent at lower thicknesses, we can vary the thickness of the resin to display shades of gray. Prior to printing, we perform a color to grayscale conversion that improves the contrast by preserving visual saliency [Gooch et al. 2005]. Figure 5c illustrates this concept. While we are currently limited to grayscale values, we anticipate that future 3D printers will support many colors, thus enabling colored content-adaptive lenticular prints. As a work around for our current printer, we could employ a multi-step printing process: in a first step, the lenses with non-regular image planes could be manufactured. Then, on a separate multi-color 3D printer, an image surface with colored pixels could be fabricated. Finally, the colored pixel surfaces could be combined onto the lens shape. If approximated color is sufficient, a simple trick can be applied to our gray-scale prints: the (color) input light field is filtered according to the lens distribution, normalized in intensity, and positioned behind the lenticular print, either on a transparency in front of the backlight or on an LCD display (which acts as a spatially-varying colored backlight). While the color plane does not coincide with the focus plane at many points, the results still show approximated color.

Lens Precision Current 3D printers have severe resolution limitations for printed optics. The smallest possible pixel and lens sizes we achieved for an Objet500 Connex 3D polymer printer were 0.2mm and 1mm respectively, though we achieved more reliable results with 0.5mm pixels and 2.5mm+ lenses: small lenses that are malformed can cause refracted rays to pass through the gaps in the image plane, causing bright spot highlights from the backlight. We successfully avoid this by printing larger lenses.

Field-of-view Baffles We print baffles between scanlines to stop light leaking through the non-planar image surface when the viewing position is far from vertically parallel. Due to the translucency of current materials and printer minimum feature sizes (0.2mm), the baffles give an appearance similar to ‘black scanline’ CRT monitors; however, printer manufacturers continue to reduce this limit and improve materials. Once printers support multiple colors, it might be possible to print content onto baffles, adding the challenge of designing a lens to focus well on both image plane and baffle.

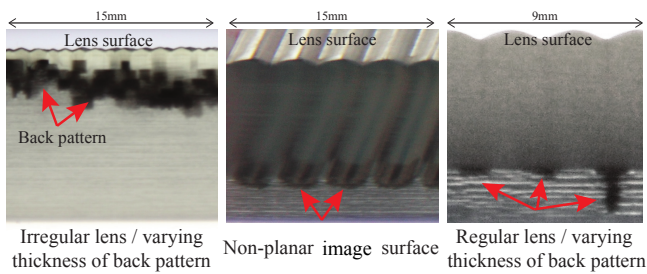


Figure 6: Irregular structure, non-planar image surfaces, and varying pixel thickness for grayscale prints. Left: 15mm; 1mm to 2mm lenses. Middle: 15mm; 3mm lenses. Right: 9mm; 3mm lenses.

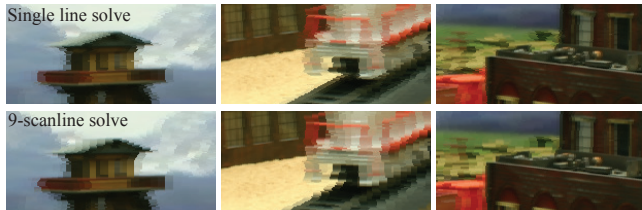


Figure 7: Effect of the multi-scanline approach for one example. The noisy streak artifacts can be reduced when solving across multiple lines, however at the cost of reducing the apparent resolution.

5.1 Discussion

While a perfectly shaped and manufactured aspherical lens will not support arbitrary dense display pixels due to its coma and spherical aberration, 20 pixels are realizable from a 10mm aspherical lens with a field of view of 30° . Furthermore, for perfectly shaped lenses the number of pixels that can be optically resolved is independent from the lens width, as long as the field of view remains constant. However, manufactured lenses are never perfect. Due to manufacturing limits, smaller lenses show higher noise and inaccuracies, which restricts the smallest possible pixel and lens size. In this case, our adaptive approach can improve the printed result. This holds especially true for the Objet500 Connex printer: although resolutions of up to $16\mu\text{m}$ of layer thickness are possible, the resulting lens shape is still inaccurate and therefore rather large lenses and image surfaces are needed. We anticipate that the resolution of future 3D printers will increase and this will allow for smaller lenses.

We currently require backlighting to achieve grayscale values. The different depths of black material refract light slightly differently, and lenses will inadvertently image different (out of focus) portions of multiple stacks of neighboring pixels. Even so, we do not believe this is a limiting factor in our prototypes as the lens size is much bigger than the difference in refraction direction. With future multi-material printers, an opaque colored image plane could be printed directly to fully avoid this problem.

While our printed results are promising, 3D printers still need to improve before being able to compete with the quality of PMMA molded lenticulars. Nevertheless, our approach shows potential and might be embedded and combined with other printed optics approaches [Willis et al. 2012]. We hope that our research into printed optics will stimulate discussion and spur 3D printer manufacturers to improve printer resolution and concurrent material range.

6 Results

We evaluate our algorithm using both simulation and physical prototype prints. Our test light fields show a wide variety of differ-

ent scenes, from low to high detail, with objects showing diffuse, specular, and transparency effects. We perform simulations assuming a perfect pinhole lens model as well as ray traces of our optimized lenses. Figure 10 shows the simulated perfect pinhole results compared to various regular lenslet arrays. Furthermore, Figure 10 shows results using ray tracing through the generated lens surface which exhibit crosstalk due to optical aberrations. The simulations were performed using one refractive index only and thus chromatic aberrations are neglected. Our adaptive lens arrays improve the perceived spatial and angular resolution simultaneously when compared to regular lens arrays. Most significantly, object borders appear much crisper due to the implicit error adaption of our algorithm. Due to the irregular arrangement of the lenses, aliasing artifacts are less noticeable at the cost of some noisy areas. To quantify the error improvement, we include PSNR comparisons between the input and output light fields in Table 1. As our algorithm computes an optimal sampling with the L2 norm, and is free to fall back to regular sampling strategies, the PSNR will always be at least as high as the best regular sampling. In our scenes, we see that our adaptive sampling improves PSNR over regular samplings.

Our approach works best for complex scenes, as such scenes can well hide the irregular lens alignment. For less complex scenes, the irregular alignment becomes more obvious, especially for round structures. Nevertheless, the perceived motion parallax is much smoother than using a regular lens distribution, which may be due to the semi-irregular sampling structure. The perceived ‘streak’ artifacts, most visible at high-contrast edges, can be reduced using the multi-scanline optimization, and Figure 7 shows this with reduced spatial noise. However, locally enforcing a regular structure reduces apparent parallax and spatial resolution. High-contrast edges are difficult to handle even with multi-scanline solving, which cannot remove all artifacts due to the angular/spatial trade-off.

To complement PSNR evaluations, we conducted a user study to perceptually assess our approach (Table 2). The study presents 10 pairwise comparisons between our content-adaptive lenslets and the highest-PSNR-ranked regular lenticular version. Our user study assessed 34 participants, most with a computer science background. The participants were asked “Which video do you prefer? Please assess both sharpness and motion smoothness (spatial resolution and angular resolution).” An introduction explained how preference is selected in the experiment. In general, the participants significantly favored our results. However, two of the scenes (‘necklace’ and ‘tarot fine’) exhibited noisy streak artifacts, and participants were split as to which choice was preferred. In cases such as these with high specularly or refraction, we cannot conclude from our study on the aliasing vs. noise trade-off. However, in other cases, our content-adaptive lenslet approach is able to increase the perceived angular and spatial resolution.

Figures 1, 6, and 9 show our prototype prints. The train scene has an input light field 1146×473 pixels large with 100 views. The physical print is $490 \times 202\text{mm}$ large. The light field is optimized for a 30° FOV, with pixels $0.5 \times 2.5\text{mm}$ large, and lenses ranging from 1mm to 12.5mm in width with the added option of placing no lens at all in pixel-sized widths. Across all scanlines, the mean lens width is 3.4mm with a std. dev. of 2.0mm, and lenses from 1mm to 7.5mm are represented (including no lens). The thickness of the print is mostly defined by the focal length of the largest lens, plus some small amount for the deepest black-level content thickness (2.1mm). With a 7.5mm largest lens, the print is 22mm thick total.

The elephant scene has an input light field 634×680 pixels large with 100 views. The physical print is $300 \times 322\text{mm}$ large. The light field is optimized for a 30° FOV, with pixels $0.4 \times 2.5\text{mm}$ large, using the same set of lenses as before. Across all scanlines, the mean lens width is 6.3mm with a std. dev. of 1.9mm, and all possible

Sampling	Amethyst	Elephant	Foyer	Jelly Beans	Lecture	Lego Bulldozer	Lego Knights	Mansion	Necklace	Pomme	Tarot Coarse	Tarot Fine	Train
Input views	17	100	150	17	150	17	17	101	17	256	17	17	100
Adaptive	31.51	24.10	30.59	35.05	28.43	26.59	26.13	18.21	19.04	33.71	22.10	26.27	26.81
Reg. 2 views	30.33	21.07	28.03	31.29	25.26	24.28	22.99	15.96	18.47	29.69	19.46	24.61	24.00
Reg. 5 views	31.42	22.64	29.61	34.76	27.87	25.89	25.90	17.39	18.09	31.43	21.66	25.23	25.72
Reg. 10 views	27.89	23.65	29.24	32.93	27.17	23.86	24.52	17.56	18.12	31.27	21.23	22.94	24.40
Reg. 20 views	N/A	22.63	27.28	N/A	24.95	N/A	N/A	16.67	N/A	29.97	N/A	N/A	22.01

Table 1: PSNR (dB) for input light fields against various regular samplings and our content-adaptive sampling (with no lens simulation). The adaptive sampling has between 2 and 50 views, though if there are fewer input views (say, 17), then we limit to this number.

	Amethyst	Elephant	Foyer	Lecture	Lego Bulldozer	Lego Knights	Mansion	Necklace	Tarot Fine	Train	All
Adaptive sampling	31	31	31	27	22	24	31	13	20	25	255
Regular sampling	3	3	3	7	12	10	3	21	14	9	85
p-value	0.000	0.000	0.000	0.000	0.016	0.001	0.000	0.055	0.151	0.000	0.000

Table 2: User study results for preference of our adaptive sampling or the regular sampling with the best PSNR. Computed using Mann-Whitney U-tests at the 5% significance level. Green marks statistical significance, where a low p-value denotes high significance.

	Volumetric	Barrier	Multi-layer	Hologram	Lenticular	Adapt. Lent.	Print proto.
Spatial Res.	High	Low	High	High	High	Low	Optimal and low
Angular Res.	High	Moderate	High	High	High	Low	High
Brightness	High	Low	Mod→High	Moderate	High	High	Moderate
Contrast	Moderate	Moderate	High	Moderate	Moderate	Moderate	Moderate
FOV	Wide	Moderate	Narrow	Wide	High	High	High
Complexity	High	Low	Moderate	High	Low	Moderate	Moderate
Flip Anim.	No	Yes	Low res.	Yes	Yes	No	No
Outdoors	Yes	Maybe	Maybe	No	Yes	Yes	Yes

Table 3: Method categorization, including a hypothetical best-case adaptive lenticular fabrication method and our printed prototypes.

lens widths are represented (including no lens). The thickness of the print with a 12.5mm largest lens is 29mm. The difference in lens choice (and so thickness) shows that, even though both light fields have the same number of input views, there is more variation in angular content appearance within the elephant scene.

The optimization and simulation framework is implemented in Matlab. The discrete optimization for 13 candidate lenses (widths between 1 and 25 pixels) can be computed in approximately 2 minutes for 1916×1272 display pixels (image surface), where 12 scanlines are computed in parallel. Due to the recursive structure of our algorithm, we expect large speedups with a native implementation. The 3D printing requires approximately 10 hours. Unfortunately, the 3D printer software cannot cope with our high resolution meshes for a full print and so we split the displays into multiple tiled strips.

6.1 Discussion and Future Work

Table 3 compares content-adaptive lenticulars to other light field display techniques (following Wetzstein et al. [2011]). Volumetric displays are complex and involve moving mechanical parts [Cosairt et al. 2007; Jones et al. 2007]. Parallax barrier displays can only offer low resolution and reduce brightness. Multi-layered displays [Wetzstein et al. 2011; Lanman et al. 2011] offer a good spatial and angular resolution, but depicting high spatial frequencies at high contrast over a large field-of-view is difficult. Further, layered displays require a certain thickness to achieve good results. Holography [Schnars and Jüpter 2005] can achieve impressive results, but requires controlled lighting and cannot be used outdoors. Standard lenticular lenses suffer from either low spatial or low angular resolution, as discussed previously. In principle, content-adaptive lenticulars offer a versatile solution and are particularly well suited

to display static 3D content in uncontrolled lighting environments, which is required for advertisements.

Our adaptive lenticulars achieve a low but balanced spatial and angular resolution, albeit in a scene-dependent manner. Brightness and contrast are similar to standard lenticular prints – at least once printing technology supports multiple colors. The supported FOV is higher than has been demonstrated in multi-layered displays. Flip animations are possible, but our adaptive approach will simply degenerate to a standard lenticular array.

Our method is limited to static content. Ideally, our approach would be combined with a display that is able to shape the lens of the lenticular on the fly in order to display dynamic content. In fact, electronically tunable LC lenses have the potential to dynamically adapt the lens arrangements, but this is future work. Furthermore, we are only supporting horizontal parallax for the following reasons. First, we can compute a global optimal solution, whereas the 2D lens packing problem is NP hard and computing a global optimum is challenging or even impossible. Second, 2D lenticular prints trade even more spatial resolution for angular, and would reduce the quality of the results. Fortunately, horizontal parallax is sufficient for stereoscopic viewing and horizontal head motion.

Current printing technology is not advanced enough to produce high-quality lenticular prints, but future printing technology, e.g., two-photon microfabrication [Sun and Kawata 2004], will likely be able to print higher-resolution lenses. For higher accuracy productions, a photo-lithographic process on silicon wafers [Wu et al. 2002] could be used as well, but the alignment of the printed surface would then have to be achieved in a second step.

7 Conclusion

We introduced content-adaptive lenticular prints. We jointly optimize both the lens configuration and the static light field content, and achieve apparent increases in spatial and angular resolution. Our simulations show improved PSNR compared to regular samplings. Participants in a user study significantly favor content-adaptive samplings. While current 3D printing techniques inhibit high-quality color results, advances in printing technology will improve the quality of our prototype lenticular prints.



Figure 8: All input light fields used for our experiments. Please see the accompanying video for results.

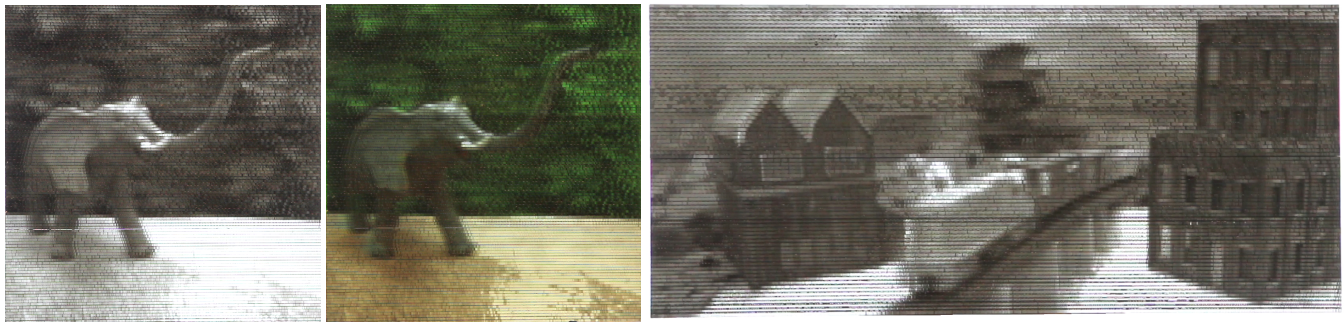


Figure 9: Printed results for the elephant (gray and approximated color) and train data set (gray). The areas of different spatial and angular resolution are clearly visible in these prototype displays. While there are still manufacturing issues related to current printing technology, the varying lens surface is demonstrated.

Acknowledgements Light fields courtesy of [UCSD/MERL Light Field Repository](#), [The \(New\) Stanford Light Field Archive](#), and [Disney Research Zurich](#) [Kim et al. 2013]. Thanks to Moira Forberg, Shinjiro Sueda, Samuel Muff, Pitchaya Sitthi-amorn, Nate Derbinsky, Kiril Vidimčec, Bernd Bickel, our study participants, and the Intel Visual Computing Institute.

References

- BERKEL, C. V. 1999. Image preparation for 3D-LCD. *Proc. SPIE Stereoscopic Displays and Virtual Reality Systems* 3639, 84–91.
- CHAI, J.-X., TONG, X., CHAN, S.-C., AND SHUM, H.-Y. 2000. Plenoptic sampling. In *Proc. SIGGRAPH*, 307–318.
- COSSAIRT, O. S., NAPOLI, J., HILL, S. L., DORVAL, R. K., AND FAVALORA, G. E. 2007. Occlusion-capable multiview volumetric three-dimensional display. *Applied Optics* 46, 1244–1250.
- COX, W. R., CHEN, T., AND HAYES, D. J. 2001. Micro-optics fabrication by ink-jet printers. *Optics and Photonics News* 12, 6, 32–35.
- CRUZ-CAMPA, J. L., OKANDAN, M. O., BUSSE, M. L., AND NIELSON, G. N. 2010. Microlens rapid prototyping technique with capability for wide variation in lens diameter and focal length. *Microelectronic Engineering* 87, 11.
- DURAND, F., HOLZSCHUCH, N., SOLER, C., CHAN, E., AND SILLION, F. X. 2005. A frequency analysis of light transport. *ACM Trans. Graph. (Proc. SIGGRAPH)* 24, 1115–1126.
- FUCHS, M., RASKAR, R., SEIDEL, H.-P., AND LENSCH, H. P. A. 2008. Towards passive 6d reflectance field displays. *ACM Trans. Graph. (Proc. SIGGRAPH)* 27, 3, 58:1–58:8.
- GOOCH, A. A., OLSEN, S. C., TUMBLIN, J., AND GOOCH, B. 2005. Color2gray: saliency-preserving color removal. *ACM Trans. Graph. (Proc. SIGGRAPH)* 24, 3, 634–639.
- HACHISUKA, T., JAROSZ, W., WEISTROFFER, R. P., DALE, K., HUMPHREYS, G., ZWICKER, M., AND JENSEN, H. W. 2008. Multidimensional adaptive sampling and reconstruction for ray tracing. *ACM Trans. Graph. (Proc. SIGGRAPH)* 27, 3, 33:1–33:10.
- HARDY, G. H., AND RAMANUJAN, S. 1918. Asymptotic formulae in combinatorial analysis. In *Proc. London Math. Soc.*, vol. 17, 75–115.
- HOLROYD, M., BARAN, I., LAWRENCE, J., AND MATUSIK, W. 2011. Computing and fabricating multilayer models. *ACM Trans. Graph. (Proc. SIGGRAPH Asia)* 30, 6, 187:1–187:8.
- ISONO, H., YASUDA, M., AND SASAZAWA, H. 1993. Autostereoscopic 3-D display using LCD-generated parallax barrier. *Electronics and Communications in Japan* 76, 7, 77–84.
- IVES, F., 1903. Parallax stereogram and process for making same. U.S. Patent No. 725,567.
- JAIN, A., AND KONRAD, J. 2007. Crosstalk in automultiscopic 3-D displays: blessing in disguise? *Proc. SPIE Stereoscopic Displays and Virtual Reality Systems* 6490, 649012.
- JANG, J.-S., AND JAVIDI, B. 2002. Improved viewing resolution of three-dimensional integral imaging by use of nonstationary micro-optics. *Optics Letters* 27, 5, 324–326.
- JANG, J.-S., AND JAVIDI, B. 2003. Large depth-of-focus time-multiplexed three-dimensional integral imaging by use of lenslets with nonuniform focal lengths and aperture sizes. *Optics Letters* 28, 1924–1926.



Input light field.



Adaptive sampling with 2 to 20 views per lens (pinhole simulation).



Adaptive sampling, 2 to 20 views per lens (raytraced lens simulation).



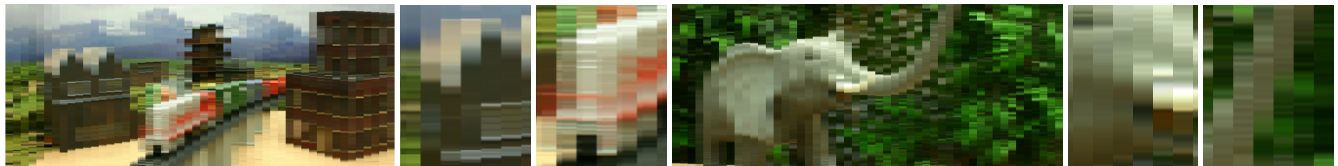
Regular sampling with 2 views per lens (pinhole simulation).



Regular sampling with 5 views per lens (pinhole simulation).



Regular sampling with 10 views per lens (pinhole simulation).



Regular sampling with 20 views per lens (pinhole simulation).

Figure 10: Spatial and angular resolution variation for the train and elephant test scenes, with the front of the house set to be at zero depth ('on' the resulting lenticular display) in the train scene and the tusk similarly in the elephant scene. The first close up shows spatial resolution improvements on the house and face, while the second shows angular improvements on the train and trunk. For regular samplings, the train scene has highest PSNR at 5 views while the elephant scene has highest PSNR at 10 views. Our supplemental material has more results.

- JOHNSON, R. B., AND JACOBSEN, G. A. 2005. Advances in lenticular lens arrays for visual display. In *Proc. SPIE* 5874.
- JONES, A., MCDOWALL, I., YAMADA, H., BOLAS, M., AND DEBEVEC, P. 2007. Rendering for an interactive 360 light field display. *ACM Trans. Graph.* 26, 3, 40:1–40:10.
- KAO, Y.-Y., HUANG, Y.-P., YANG, K.-X., CHAO, P. C.-P., TSAI, C.-C., AND MO, C.-N. 2009. An auto-stereoscopic 3D display using tunable liquid crystal lens array that mimics effects of GRIN lenticular lens array. *SID Symposium Digest of Technical Papers* 40, 111–114.
- KIM, Y., PARK, J.-H., MIN, S.-W., JUNG, S., CHOI, H., AND LEE, B. 2005. Wide-viewing-angle integral three-dimensional imaging system by curving a screen and a lens array. *Applied Optics* 44, 546–552.
- KIM, Y., KIM, J., KANG, J.-M., JUNG, J.-H., CHOI, H., AND LEE, B. 2007. Point light source integral imaging with improved resolution and viewing angle by the use of electrically movable pinhole array. *Optics Express* 15, 26, 18253–18267.
- KIM, Y., HONG, K., AND LEE, B. 2010. Recent researches based on integral imaging display method. *3D Research* 1, 17–27.
- KIM, S.-C., KIM, C.-K., AND KIM, E.-S. 2011. Depth-of-focus and resolution-enhanced three-dimensional integral imaging with non-uniform lenslets and intermediate-view reconstruction technique. *3D Research* 2, 2, 6.
- KIM, C., ZIMMER, H., PRITCH, Y., SORKINE-HORNUNG, A., AND GROSS, M. 2013. Scene reconstruction from high spatio-angular resolution light fields. *To appear ACM Trans. Graph. (Proc. SIGGRAPH)*.
- KWEON, G.-I., AND KIM, C.-H. 2007. Aspherical lens design by using a numerical analysis. *Journal of the Korean Physical Society* 51, 1, 93–103.
- LANMAN, D., HIRSCH, M., KIM, Y., AND RASKAR, R. 2010. Content-adaptive parallax barriers: optimizing dual-layer 3D displays using low-rank light field factorization. *ACM Trans. Graph. (Proc. SIGGRAPH)* 29, 6, 163:1–163:10.
- LANMAN, D., WETZSTEIN, G., HIRSCH, M., HEIDRICH, W., AND RASKAR, R. 2011. Polarization fields: dynamic light field display using multi-layer LCDs. *ACM Trans. Graph. (Proc. SIGGRAPH)* 30, 6 (Dec.), 186:1–186:10.
- LEHTINEN, J., AILA, T., CHEN, J., LAINE, S., AND DURAND, F. 2011. Temporal light field reconstruction for rendering distribution effects. *ACM Trans. Graph. (Proc. SIGGRAPH)* 30, 4, 55:1–55:12.
- LIPPMANN, G. M. 1908. La photographie integrale. *Comptes-Rendus* 146, 446–451.
- LUEDER, E. 2012. *3D Displays*. Wiley.
- NASHEL, A., AND FUCHS, H. 2009. Random Hole Display: A non-uniform barrier autostereoscopic display. In *3DTV Conference: The True Vision – Capture, Transmission and Display of 3D Video*, 1–4.
- PAPAS, M., JAROSZ, W., JAKOB, W., RUSINKIEWICZ, S., MATUSIK, W., AND WEYRICH, T. 2011. Goal-based caustics. *Computer Graphics Forum* 30, 2, 503–511.
- PAPAS, M., HOUIT, T., NOWROUZEZHAI, D., GROSS, M., AND JAROSZ, W. 2012. The magic lens: Refractive steganography. *ACM Trans. Graph. (Proc. SIGGRAPH Asia)* 31, 6, 186:1–186:10.
- PARK, J.-H., KIM, J., KIM, Y., AND LEE, B. 2005. Resolution-enhanced three-dimension / two-dimension convertible display based on integral imaging. *Optics Express* 13, 1875–1884.
- PERLIN, K., PAXIA, S., AND KOLLIN, J. S. 2000. An autostereoscopic display. In *Proc. of SIGGRAPH*, 319–326.
- PETERKA, T., KOOIMA, R. L., SANDIN, D. J., JOHNSON, A., LEIGH, J., AND DEFANTI, T. A. 2008. Advances in the dynamic solid-state dynamic parallax barrier autostereoscopic visualization display system. *IEEE T. VIS. COMPUT. GR.* 14, 3, 487–499.
- RAMACHANDRA, V., HIRAKAWA, K., ZWICKER, M., AND NGUYEN, T. 2011. Spatio-angular prefiltering for multiview 3D displays. *IEEE T. VIS. COMPUT. GR.* 17, 5, 642–654.
- SAID, A., AND TALVALA, E.-V. 2009. Spatial-angular analysis of displays for reproduction of light fields. *Proc. SPIE* 7237.
- SAJADI, B., GOPI, M., AND MAJUMDER, A. 2012. Edge-guided resolution enhancement in projectors via optical pixel sharing. *ACM Trans. Graph.* 31, 4 (July), 79:1–79:122.
- SCHNARS, U., AND JÜPTER, W. 2005. *Digital Holography: Digital Hologram Recording, Numerical Reconstruction, and Related Techniques*. Springer.
- SMITH, W. J. 2007. *Modern optical engineering*. SPIE Press.
- SUN, H.-B., AND KAWATA, S., 2004. Two-photon photopolymerization and 3d lithographic microfabrication.
- TAKAHASHI, H., FUJINAMI, H., AND YAMADA, K. 2006. Wide-viewing-angle three-dimensional display system using hoe lens array. *Proc. SPIE* 6055, 60551C–1–60551C–9.
- UEDA, K., KOIKE, T., TAKAHASHI, K., AND NAEMURA, T. 2008. Adaptive integral photography imaging with variable-focus lens array. *Proc. SPIE* 6803.
- WETZSTEIN, G., LANMAN, D., HEIDRICH, W., AND RASKAR, R. 2011. Layered 3D: Tomographic image synthesis for attenuation-based light field and high dynamic range displays. *ACM Trans. Graph. (Proc. SIGGRAPH)* 30, 4, 95:1–95:12.
- WETZSTEIN, G., LANMAN, D., HIRSCH, M., AND RASKAR, R. 2012. Tensor displays: Compressive light field synthesis using multilayer displays with directional backlighting. *ACM Trans. Graph. (Proc. SIGGRAPH)* 31, 4, 80:1–80:11.
- WILLIS, K., BROCKMEYER, E., HUDSON, S., AND POUPYREV, I. 2012. Printed optics: 3d printing of embedded optical elements for interactive devices. In *ACM Symposium on User Interface Software and Technology*, 589–598.
- WU, M.-H., PARK, C., AND WHITESIDES, G. 2002. Fabrication of arrays of microlenses with controlled profiles using gray-scale microlens projection photolithography. *Langmuir* 18, 24.
- ZEBRA IMAGING, 2013. ZScape® digital holographic prints. <http://www.zebraimaging.com>.
- ZWICKER, W., MATUSIK, W., DUR, F., PFISTER, H., ZWICKER, M., MATUSIK, W., DURAND, F., AND PFISTER, H. 2006. Antialiasing for automultiscopic 3D displays. In *Eurographics Symposium on Rendering*, 73–82.
- ZWICKER, M., VETRO, A., YEA, S., MATUSIK, W., PFISTER, H., AND DURAND, F. 2007. Resampling, antialiasing, and compression in multiview 3-D displays. *IEEE Signal Processing Magazine* 24, 6 (Nov.), 88–96.